Chapter 16

Cerebral Monitoring and Surveillance Using High-Resolution Functional Optical Imaging

Anthony D. Uglialoro, Douglas S. Pfeil, Tigran Gevorgyan, Harry L. Graber, Yong Xu, Sundeep Mangla, Frank C. Barone, Jenny Libien, Jean Charchaflieh, John G. Kral, Sergio A. Ramirez, LeRone Simpson, Daniel C. Lee, and Randall L. Barbour

Abstract

Near-infrared (NIR) optical techniques, using large-area sensing arrays that provide for transcranial measures of cortical function, are finding increasing use for functional assessment of brain activity. In this chapter, we review current capabilities of these methodologies and describe their application to an in vivo large animal model, Bonnet macaque, for the purpose of imaging hemodynamic responses to clinically significant events, including detection of cerebral ischemia and hemorrhage. The described methodology outlines the technology and method of high-density diffuse optical tomography (DOT), as explored using recently developed analysis resources whose accuracy is independently validated. Also discussed are solutions to commonly encountered problems related to data collection and analysis.

Key words Diffuse optics, Diffuse optical imaging, Near-infrared spectroscopy (NIRS), Topography, Diffuse optical tomography (DOT), Cerebral monitoring and surveillance

1 Introduction

Disturbances in brain function can have lifelong consequences. Tools available for assessment of brain function vary in their sensitivity to underlying physiology or pathology, as well as their technology footprints. Together these factors can significantly influence the clinical usability of a given technology. Ideally, in addition to providing clinically relevant information (e.g., presence, position, and spatial extent of pathologies), the considered technology would have favorable attributes that support its usability, including but not limited to, system size, cost, noninvasiveness, safety, and easy-of-use.

Anthony D. Uglialoro and Douglas S. Pfeil have contributed equally to this chapter.

Mingrui Zhao et al. (eds.), *Neurovascular Coupling Methods*, Neuromethods, vol. 88,
DOI 10.1007/978-1-4939-0724-3_16,

The noninvasive methods available for assessing brain function include various imaging technologies that are well-suited for defining brain anatomy, the impact of acute events, and the brain's principal functional properties. Chief among the anatomical imaging technologies are X-ray computed tomography (CT) and magnetic resonance imaging (MRI). In cases of trauma or cerebral vascular accidents, non-contrast CT imaging is the preferred modality [1]. Owing to its enhanced specificity, MRI is often used in non-acute situations for further investigation of cerebral pathologies, including the detection of tumors and monitoring the progression of multiple sclerosis or encephalopathy [2, 3].

Several direct and indirect clinical neuromonitoring techniques are currently available for examining functional brain activity. These technologies have documented that brain activation and many pathologies (e.g., Alzheimer's [4], Parkinson's diseases [5], and cognitive impairment due to traumatic brain injury [6]) produce spatially distributed and temporally varying responses. Techniques that provide direct information of neuron-derived brain activity include electroencephalography (EEG) [7, 8] and its magnetic equivalent, magnetoencephalography (MEG) [9]. These methods provide a high degree of temporal resolution but have markedly reduced spatial resolution compared to the principal anatomical imaging techniques (MRI, CT). Indirect methods for monitoring brain activity have been derived from measures of the hemodynamic response coupled to neuroactivation [10], as well as from associated metabolic transformations that can be assessed by the method of positron emission tomography (PET) [11]. Among the former is the method of functional Magnetic Resonance Imaging (fMRI) [12, 13], which is based on neuroactivation-induced variations in the concentration of (paramagnetic) deoxyhemoglobin [14].

At present, while each of the above techniques has its distinct advantages for monitoring brain function, the direct methods (EEG, MEG) tend to have limited spatial resolution, whereas the indirect methods are restricted to inferring neuronal activity after it has been filtered through a complex neurovascular coupling mechanism. As discussed subsequently, over the past decade a new approach for indirect monitoring of brain function has emerged that offers the potential for wide use in many clinical specialties and subspecialties, owing to its favorable technology footprint and its sensitivity to important clinical disturbances.

1.1 Optical Imaging: Technology and Capabilities

Extensive clinical experience with pulse oximetry has demonstrated that the optical method is well-suited for measuring important features of the hemoglobin signal. Favoring its use is compact and low-cost sensing hardware, and its ability to noninvasively detect temporal variations in the content and oxygenation level of hemoglobin (Hb) with high sensitivity. In turn, the Hb content and oxygenation are closely tied to tissue perfusion, and this has prompted many to exploit the inherent flexibility of optical methods for potential clinical applications. Two distinct approaches have emerged. First, low-density sensing arrays (i.e., delivering light into and detecting it from the head at only a few—typically 1–4—locations) have been adopted as a tool for tissue oximetry [15–19]. Second, the extension of these methods to include high-density arrays (i.e., involving larger numbers of light delivery and detection points, distributed over a larger area), together with use of more advanced mathematical treatment of the data, has allowed for the development of new classes of functional imaging techniques.

Intrinsic optical imaging is an example of a method having high spatial resolution. This technique employs broad-area illumination of an exposed brain preparation, combined with use of high-resolution digital cameras. While this technique is mainly used as an experimental tool, it has been shown capable of real-time measures of both the intrinsic hemodynamic signal and membrane potential changes due to the neuronal response, especially when it is used in combination with voltage-sensitive dyes [20].

The use of near-infrared (NIR) spectroscopic methods to explore the temporal dynamics of the Hb signal in a closed cranium are built upon an observation made by Jöbsis in 1977 [21]. More than a decade later, this observation motivated two distinct technology development efforts that shared the goal of noninvasive functional imaging.

Beginning in the late 1980s, Barbour and coworkers showed that model-based methods for analyzing light transport in diffusing media can be adopted as a strategy for spatially resolving local variations in the oxygenation states of heme-containing proteins, principally Hb [22, 23]. The notable advance here was the recognition that low-resolution images of spatial features of subsurface structures can be recovered from measurements of the emission profile of *diffusely scattered* light. Prior to these demonstrations, it had been assumed that these features were irretrievably obscured due to the intense scattering of light by tissue. The spirit of this technique, known as *diffuse optical tomography*, is similar to other methods (i.e., X-ray CT), in that image formation is based on the treatment of multi-view measures. A principal difference is that scattering causes light to assume probabilistic paths (unlike the straight-line paths taken by X-rays) whose particulars are dependent on features of the medium and details of illumination and detection [24]. These particulars, however, can be explicitly considered using mathematical models [25]. These early studies coincided with groundswell of related activities throughout the 1990s by other groups [26–31] that built on the many ways optical techniques can be employed to examine features of dense scattering media. Among these was the evidence that use of arrays of emitters and detectors can detect local variations in the hemodynamic response to neuroactivation (see Ferrari and Quaresima for review of the historical development of functional near-infrared spectroscopy (fNIRS) [32]).

These considerations have led to development of a series of instrumentation platforms (see Note 1) that ultimately rely on more simplified mathematical treatment of the data than that used for tomography studies to explore spatiotemporal features of the Hb signal. This technique, known as *optical topography* [33], maps weighted volume-averaged measures of the Hb signal to the surface of the scalp or, by linear projection, to the cortex (see Fig. 3). Similar to the tomography approach, the detected signal is diffusely scattered. Both techniques employ grossly similar instrumentation, but differ in the density of sensing elements deployed, with higher-density arrays used for tomography and, as indicated, differ in the approaches used for data analysis. For both approaches, light delivery can be accomplished either through use of intervening optical fibers or by placement of miniaturized illumination and detection elements directly on the scalp. Typical for topography studies is the use of a rectilinear array having ~3 cm spacing between the elements; tomography arrays detect re-emitted light at multiple distances from any one source (see Note 1 for a description of trade-offs between technology complexity and derived information, for topographic and tomographic measures).

Underscoring the attractiveness of the optical method is its use of non-damaging energy sources and instrumentation having form factors that can be made compact, even wearable [34]. Also, because Hb is the dominant time-varying optical attenuator in tissue, many applications that are based on examination of this signal can be explored. For instance, a frequent concern in clinical medicine is whether perfusion of the brain has been compromised. While there have been numerous studies of the use of low-density tissue oximetry as a monitoring tool, the use of large-area arrays for assessment of brain function in clinical settings has been thus far underutilized, owing to the need for more refined system designs that are appropriate for these settings.

As a first step in bridging this gap, in this chapter we describe a general methodology for using the tomography approach to investigate acute vascular events having clinical significance, and we demonstrate its application to a large animal model. Specifically examined here were the responses to acute cerebral vascular maneuvers, such as injection of a contrast agent, and the response to clinically relevant events, such as induced cerebral ischemia or subarachnoid hemorrhage (SAH).

Key elements of the method are the use of a high-density sensing array, inversion of measured signals based on a group-averaged anatomical atlas, and use of an integrated analysis environment to produce a three-dimensional (3D) image time series of various components of the Hb signal. Also presented are the results from independent studies that validate the optical findings based on use of radiological and postmortem histological techniques.

2 Methods

2.1 Animal Preparation

2.1.1 Bonnet Macaque

The arterial vasculature of the Bonnet macaque brain is anatomically similar to that of the human brain. (The most apparent difference is that the macaque has a single anterior cerebral artery (ACA), while the human has distinct left and right ACAs.) This has led a number of investigators to employ the macaque as an animal model for stroke and other cardiovascular research.

For the current studies, subjects investigated were adult male macaques weighting approximately 7 kg, aged 5–6 years. A total of five animals were studied under an IACUC-approved protocol. For purposes of documenting the method of high-resolution functional optical imaging, results from a single animal are reported.

2.1.2 Anesthesia and Setup

Using standard animal anesthesia protocols, the animal was sedated and intubated [35]. Once this was established, hemodynamic monitors were applied that recorded blood pressure, oxygen saturation (SaO_2), and electrocardiography (ECG) throughout experimentation. An intra-venous (IV) catheter was inserted for administration of fluids and medications, along with an arterial line to monitor the blood pressure more accurately.

In order to gain access into the arterial system for cerebral angiography and for temporary occlusion of the cerebral vessels, a femoral artery catheter sheath [5 Fr (i.e., 5/3 mm)] was inserted in the groin of the animal and secured using standard cut-down surgical technique.

2.1.3 Exposure of Scalp

In order to apply the optical interface, the overlying tissues including the skin and head muscles were removed using standard surgical techniques. A 4 × 5 cm area in the mid-frontal–parietal region of the scalp of the animal was reflected, exposing the skull. This was performed to achieve optimal optical penetration to subsurface tissues. Scalp reflection was necessary in this macaque model because the very thick (1–2 cm) frontalis muscle would otherwise absorb most of the light. In human studies, significant optical penetration is achieved without any need for equivalent procedures, because the overlying tissues are much thinner. Please see Note 2 for a description of expected influence of superficial tissues to applied optical measures.

2.2 Equipment Setup for Functional Optical Imaging

2.2.1 Preparation for Optode Interface and Array

The optode–tissue interface was custom-designed for the animals. The physical support structure for the optodes was a 7 cm diameter, 9 mm thick sheet of black Delrin® that was machined to provide a pattern of hexagonal segments to allow close fitting between the optical hardware and the skull. Shown in Fig. 1 is a photograph of the optode holder secured to the skull of the anesthetized animal. The optode interfaces containing the optical fibers were placed

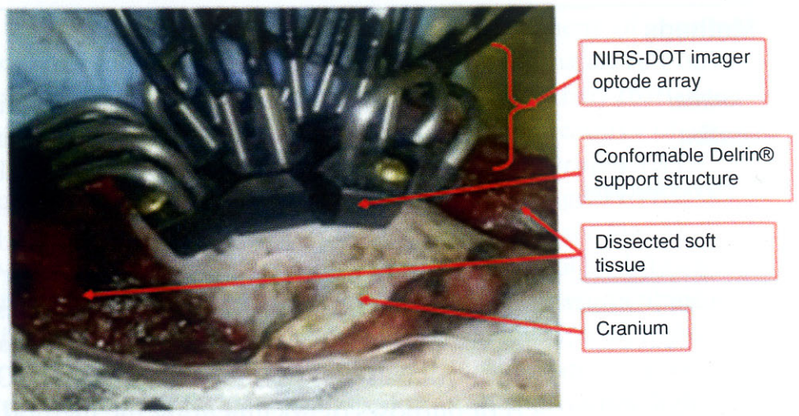

Fig. 1 Photograph of fNIRS optode holder secured to the Bonnet macaque's skull after reflection of the overlying soft tissues

over the exposed 4×5 cm skull surface and secured using small screws. The optodes were positioned 10 mm apart. Shown in Fig. 2 is a schematic layout of the optode array. There were 9 illumination sites, which also served as detection sites, and 21 detection-only sites, for a total of 30 detectors. Thus there were 9×30=270 data acquisition channels in total. The co-located design was implemented by combining source fibers with a halo of detector fibers to produce a common end.

2.2.2 Instrumentation and Data Collection

Data collection was achieved using a continuous wave (CW)-NIRS imaging system (DYNOT, NIRx Medical Technologies). After the optode array within its holder was secured to the skull using small screws, the amplification settings for each source–detector pair were established using an automated procedure that sweeps the amplifier gain over the full sensing range available (nine decades) and identifies the gain that yields an optimal signal without saturation of the detection circuitry. These settings are stored in instrument memory and successively accessed for each illumination site, thereby achieving real-time adaptive gain control.

Time-multiplexed illumination (i.e., each source is sequentially illuminated) was performed by optically combining light from two diode lasers, operating at 760 and 830 nm, into small-diameter fiber bundles (~3 mm) that terminate on the skull. Light received into the fiber bundles was measured by parallel readout from the light sensing elements (i.e., silicon photodiodes). The sensing array was read out at the rate of 8 Hz. System control, real-time data viewing, and data storage are performed using a LabView (National Instruments Corporation, www.ni.com) interface. See Schmitz et al. [36, 37] for details of system design and operation. See Note 3 for a discussion of illumination-detection strategies.

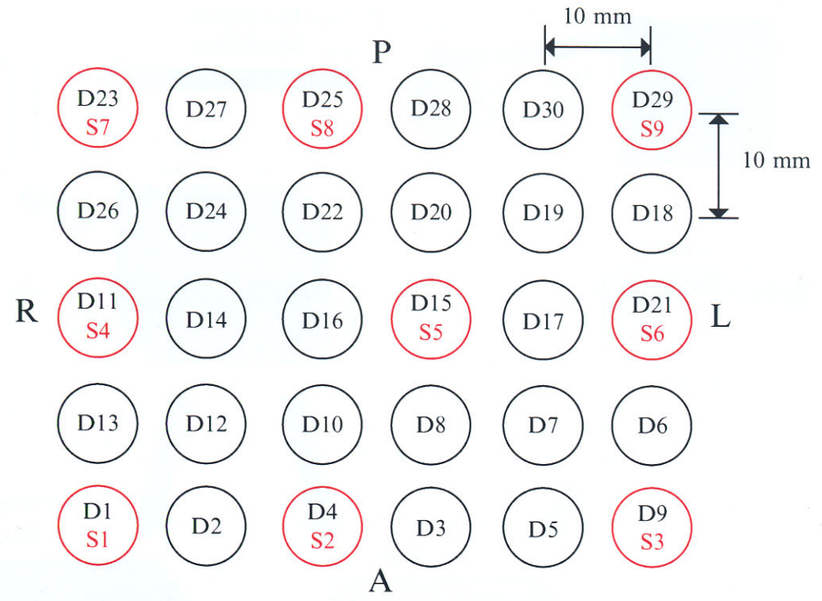

Fig. 2 A schematic layout of the optode array. *Black numbers* represent detectors and *red numbers* represent light sources. Letters denote orientation: (A): anterior; (L): left; (P): posterior, (R): right side

2.3 Angiography and Cerebral Vascular Manipulation

After a baseline recording of approximately 10 min, intra-arterial digital subtraction angiography (DSA) of the brain was performed to identify the correct cerebral vessel in which to induce temporary ischemia. In this case, the middle cerebral artery (MCA), which is a continuation of the internal carotid artery (ICA), was located using a 5-Fr diagnostic catheter with the use of iodinated contrast (Iohexol 300 mgI/mL) to assist in the navigation to the MCA. For the purposes of establishing regional acute cerebral ischemia, an occlusive angioplasty microcatheter [2.7 Fr (i.e., 0.9 mm outer diameter)] was threaded through the femoral artery sheath under radiological guidance and then wedged at the origin of the MCA. Before the occlusion attempts, verapamil, a drug known for its vasodilatory effects, was locally injected into the right ICA/MCA. Several contrast injections were performed to assist the guidance of the catheter to the point of occlusion. The microcatheter was left in place for 3 h, then removed to restore blood flow to the occluded area. The specific protocol implemented here was modified in response to initial difficulties in guiding the microcatheter to the initial planned cerebral vessel (right MCA) as a consequence of vasospasm. As a result, the contralateral (left) ICA was occluded instead.

2.4 MR Validation and Postmortem Studies

After 1 h of arterial reperfusion, the NIRS recording was stopped and the animal was transported to the imaging suite. Standard stroke protocol sequences including diffusion, T2, T1, and fluid-attenuated inversion recovery (FLAIR) were performed.

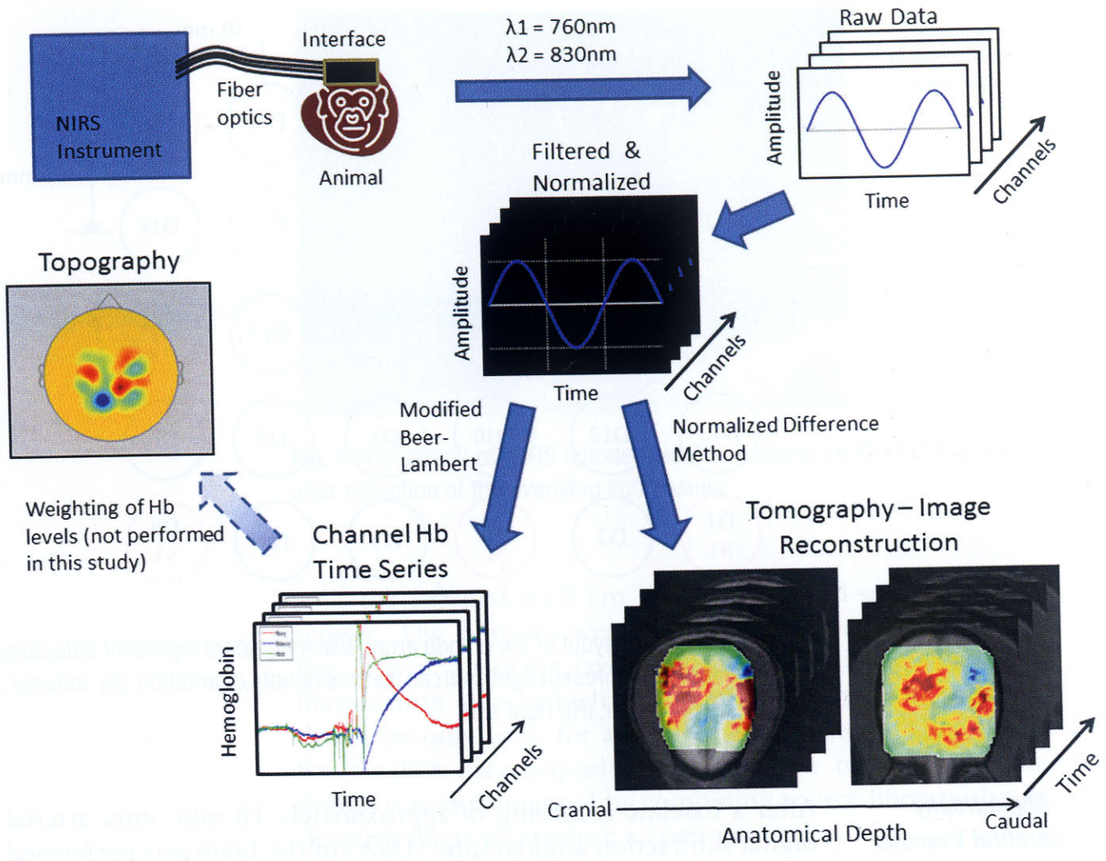

Fig. 3 A schematic depicting the data processing steps involved in NIRS measurements

The animal was then transported to the autopsy room, where euthanasia was performed using pentobarbital, 120 mg/kg, IV. At the conclusion of euthanasia, the brain was removed and fixed in 10 % buffered formalin for at least 2 weeks, after which coronal sections were cut at approximately 5 mm intervals. Brain regions corresponding to the center of the infarct, as determined by the postsurgical radiological data and from the corresponding location on the contralateral side, were submitted for routine tissue processing and paraffin embedding. Hematoxylin and eosin-stained sections, each 8–10 μm in thickness, were then examined by light microscopy.

2.5 Analysis of NIRS Measures and Image Reconstruction

Wavelength-dependent time-series measures obtained from the sensing array may be processed in two principal ways: either through the Modified Beer–Lambert Law (MBLL) [39] to yield channel-based hemoglobin time series (the first step in topography), or through image reconstruction algorithms to yield 3D Hb time series (tomography). See Fig. 3 for a schematic of data processing steps.

The Beer-Lambert Law (Absorbance = [ε]×[Concentration]×[Length]) is commonly used in spectrophotometric determinations of the concentrations of substances suspended in clear media (e.g., protein in an aqueous solution or the concentration of DNA). In optical monitoring applications that are based on low-density arrays or on optical topography, Hb concentrations are estimated by using a modified Beer-Lambert Law that takes account of the increased light propagation distance resulting from photon scattering in tissue. This correction is called the differential pathlength factor (DPF) [38]. Thus, the MBLL can be written as:

$$\log \frac{I(j)}{I_{bl}} = \varepsilon \times \Delta c(j) \times (\mathrm{DPF} \times l),$$

where $I(j)$ is the detected signal value in the jth measurement frame and I_{bl} is the average value of the signal detected over a selected "baseline" time interval. ε is the extinction coefficient of the chromophore [oxy- and deoxyhemoglobin (Hb_{oxy}, Hb_{deoxy})] and l is the linear distance between light source and detector. Because it can be difficult to measure the precise value of light intensity entering the tissue, it is convenient to report Hb concentrations as changes with respect to the baseline value (ΔHb).

Image reconstruction, on the other hand, uses a different method to calculate ΔHb values. The algorithm we used for reconstruction is called the normalized difference method (NDM) [67]. In this method, the differences between predicted (forward model) and measured channel data are related to changes in the interior optical properties (e.g., absorption) of the investigated medium, with respect to a defined reference medium. The Jacobian operator [67] and reference detector values were computed prior to data analysis, from forward-model solutions to the diffusion equation, using a 3D tessellated and segmented group atlas. See Note 4 for discussion of forward modeling techniques.

For this experiment, image reconstruction was performed via the following three-step process:

Step 1: Raw data was subjected to a low-pass filter (0.2 Hz cutoff) and normalized to its temporal mean value, separately for each data acquisition channel and each measurement wavelength.

Step 2: Using a 3D tessellated and segmented group monkey atlas, whose details are described below, the Jacobian operator and reference detector values were computed.

Step 3: The quantities computed in Steps 1 and 2 were subsequently processed by applying the NDM to generate a wavelength-dependent 3D image time series of the recovered absorption coefficients. Conversion of these spatial maps to corresponding maps of the hemoglobin components was

accomplished using methods described by Schmitz et al. [39]. See Note 5 for discussion of limitations of linear inverse solvers applied to recovery of image time series.

Steps 1 and 3 were accomplished using routines available in the NAVI (*N*ear-infrared, *A*nalysis, *V*isualization, and *I*maging) software package [40]. This MATLAB (The MathWorks, Inc., Natick, MA, USA)-based software is freely available and can be downloaded from the NITRC website at http://www.nitrc.org/projects/fnirs_downstate. Forward solutions to the diffusion equation (Step 2) were obtained using a previously described finite element method (FEM)-based solver written in Fortran [41]. To accomplish this, first a tetrahedral FEM mesh was applied to the atlas, followed by assignment of optical coefficients to the segmented anatomy as described in references [42, 43]. To more accurately reflect the conditions of surgery, numerical solutions to the forward problem were obtained by carefully locating the sensor positions onto the skull of the atlas, rather than to the scalp.

2.5.1 Generation of a Hybrid Group Atlas

Figure 4 illustrates the principal steps involved in generating the hybrid group atlas used in these studies. Briefly, by carefully measuring the dimensions along the principal axes from MRI images of a single-animal brain and from a group-averaged brain obtained from the literature [44], and then executing an affine transformation [45], we substituted the group brain for the individual brain to

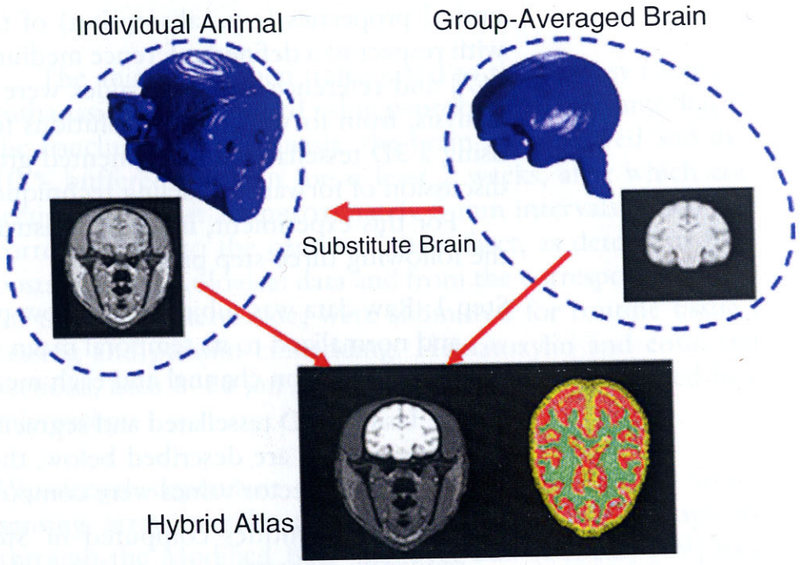

Fig. 4 A schematic showing the process used to create the macaque atlas. Information from a group-averaged brain is superimposed onto an individual MRI scan to yield the hybrid atlas. The image in the *bottom right* shows one of the segmented and tessellated slices from the atlas

yield a hybrid atlas. As reported by McLaren et al. [44], the group-averaged brain was derived from 80 adult male and 32 adult female Rhesus macaque monkeys, which are anatomically similar to Bonnet macaques. Group atlases are frequently adopted in order to minimize biases inherent to specific anatomical features of an individual, as well as to provide for comparisons across platforms, sensing modalities, and other atlases.

3 Results of the Applied Methodology

Shown in Figs. 5 and 6 are cross-sectional views of reconstructed 3D images of the Hb response to the vascular events described above. Figure 5a shows an axial view of the amplitude of the ΔHb_{oxy} image obtained during the baseline period (sampled at 20 min). Figure 5b is the coronal view obtained from the transect indicated in Fig. 5a. Both images reveal a relatively low-amplitude spatial variation in signal contrast. Shown in Fig. 5c, d are corresponding

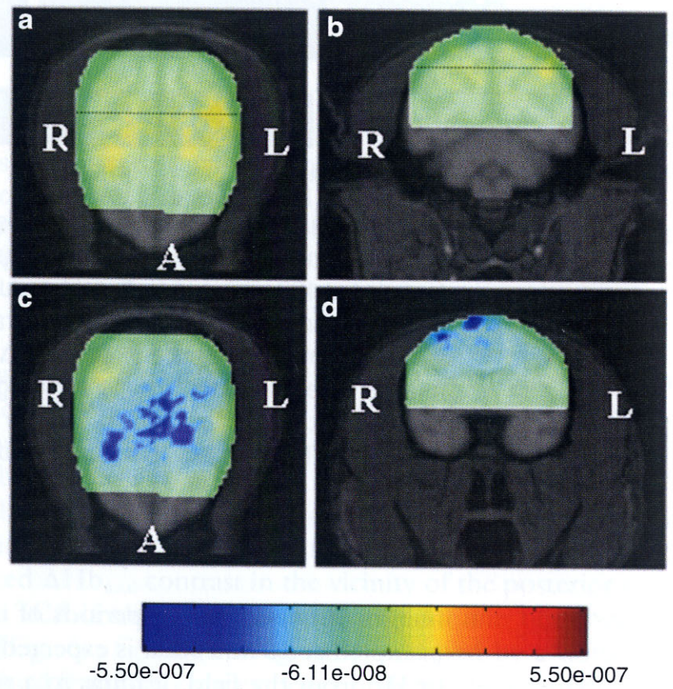

Fig. 5 Axial and corresponding coronal cross-sectional image views of ΔHb_{oxy} (mol/L) during (**a**) and (**b**): baseline and (**c**) and (**d**): post-injection of contrast agent (approximately 10 s post-injection). (**a**, **b**) reveal a relatively low-amplitude spatial variation in signal contrast, while (**c**, **d**) reveal displacement of hemoglobin from the field leading to a reduced ΔHb_{oxy} signal (*blue* contrast feature). *Dotted lines* in (**a**, **b**) indicate the intersections among the plotted two-dimensional (2D) sections

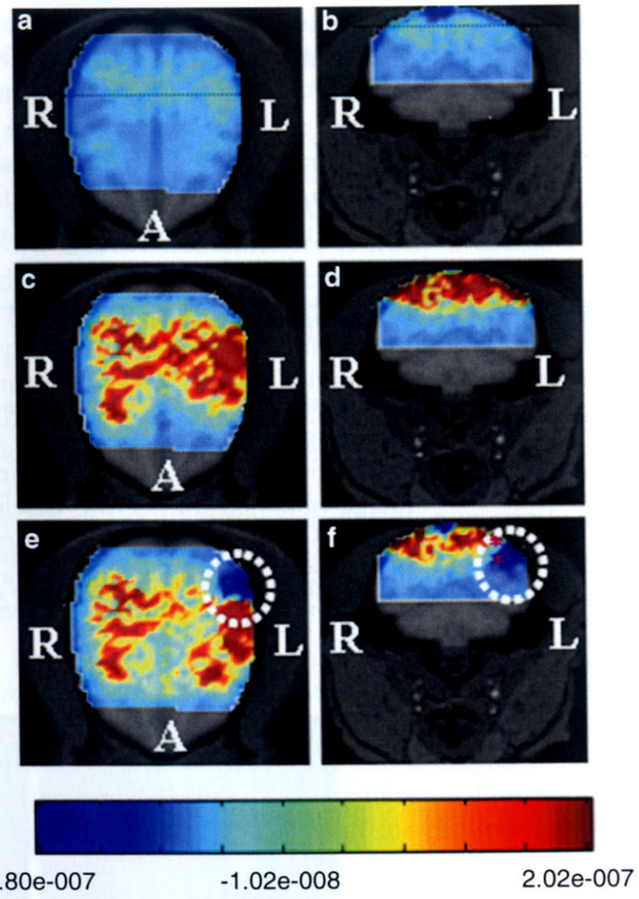

Fig. 6 Axial and corresponding coronal cross-sectional image views of ΔHb_{total} (mol/L) obtained during the (**a**, **b**): baseline (sampled at 20 min), (**c**, **d**): post-SAH (sampled at 125 min), and (**e**, **f**): post-occlusion (sampled at 166 min, approximately 40 min post-occlusion) of the cerebral vessel. Subarachnoid hemorrhage is revealed by the presence of elevated ΔHb_{total} signal (*red* contrast feature). A region of reduced ΔHb_{total} signal is highlighted by the *dotted circle* (*blue* contrast feature). *Dotted lines* in (**a**, **b**) indicate the intersections among the plotted 2D sections. The *asterisks* in (**f**) mark the pixels represented in Fig. 7

images obtained during periods of injection of the contrast agent (sampled at 90 min) that is expected to cause a bolus displacement of Hb from the field, leading to a reduced signal, as indicated by the areas of dark blue.

Shown in Fig. 6 are similar views of images of the ΔHb_{total} ($\Delta Hb_{total} = \Delta Hb_{oxy} + \Delta Hb_{deoxy}$) obtained during the baseline period (sampled at 20 min, Fig. 6a, b), post-SAH (sampled at 125 min, Fig. 6c, d), and post arterial occlusion (sampled at 166 min, Fig. 6e, f) periods. Comparison of the image features reveals three principal findings. First, owing to a large rapid change in the recorded

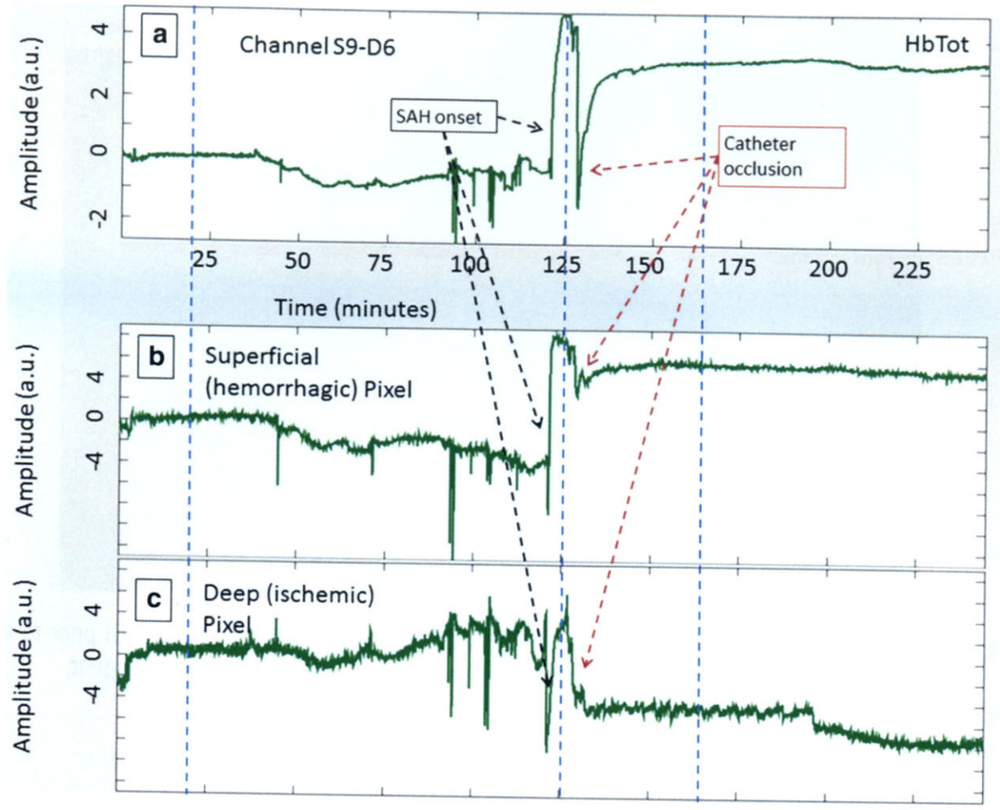

Fig. 7 (**a**) S9-D6 channel data for ΔHb_{total} (see Fig. 2 for channel location). Both the onset of SAH and catheter occlusion are visible. (**b**) Time-series data for a pixel (from the reconstructed image) just under the skull. Note the SAH is prevalent but catheter occlusion only produces a small change. (**c**) Time-series data for a pixel in the ischemic region. Note there is very little change in ΔHb_{total} at the time of the SAH, but a decrease corresponding to catheter occlusion is prevalent. The *blue dashed lines* correspond to the times sampled in Fig. 6

optical signals during manipulation of the catheter in attempts to occlude the MCA (see Fig. 7), a rupture of one of the cerebral vessels was suspected and was concurrently confirmed by DSA, and later by postsurgical radiology and postmortem evaluation. This is revealed by the presence of elevated ΔHb_{total} signal in the recovered images (red contrast feature, Fig. 6c, d). Second, a region of reduced ΔHb_{total} contrast in the vicinity of the posterior tributaries of the ICA is seen after approximately 40 min of ischemic occlusion [Fig. 6e, f (affected region is indicated by a dotted circle)]. The third feature is clear evidence of depth discrimination between the more superficial confinement of hemorrhage and areas of ischemia at greater depths in the brain. Additionally, it is instructive to compare reconstructed time series for selected pixels in these affected regions (denoted by asterisks in Fig. 6f) to the response of a source–detector pair positioned near the left frontal–parietal region (S9-D6, Fig. 2). The MBLL was used to compute the ΔHb_{total} time series for this channel. These results are shown in Fig. 7.

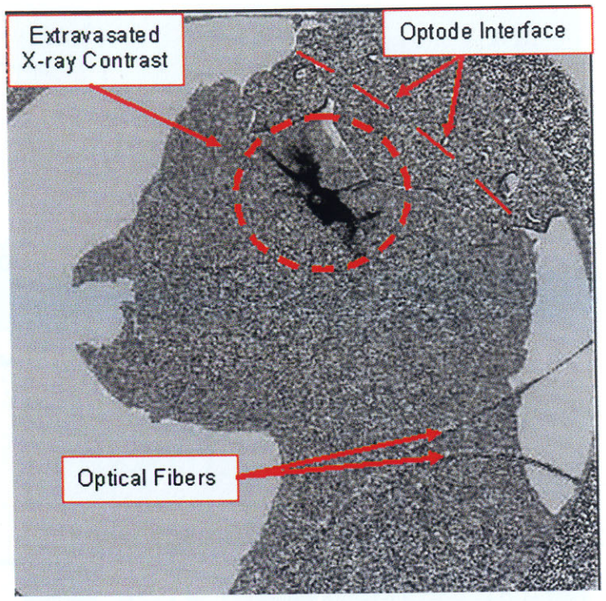

Fig. 8 Lateral DSA demonstrating right ICA perforation and SAH prior to subsequent occlusion. Dark material is extravasated X-ray contrast agent

Figure 7a reveals that at approximately 120 min, the ΔHb_{total} signal rapidly increases, which is indicative of SAH. Additionally, a drop at 130 min marks the time of occlusion by the microcatheter. However, interpretation of the data from Fig. 7a would be difficult without prior knowledge of the events of the experiment. Even after catheter occlusion, ΔHb_{total} values remain above baseline. The extent of the ischemia in the deeper tissue is not fully revealed. Figure 7b, c show the reconstructed ΔHb_{total} times series for a pixel just under the skull and a pixel about 1 cm deeper in the brain, respectively. These two time series demonstrate how the different regions of the brain tissue are affected during this experiment. Figure 7b clearly shows the increased ΔHb_{total} signal corresponding to the SAH, while very little change is evident during catheter occlusion. Figure 7c shows the opposite. This is a clear demonstration of the utility provided by image reconstruction.

Corroborating evidence in support of the optical findings, obtained by DSA and MRI, is shown in Figs. 8 and 9. Figure 8 reveals a high-contrast feature showing extravasation of X-ray contrast agent, indicating cerebral vessel perforation. Figure 9 reveals a region of hyperintensity as seen by FLAIR MRI, confirming that ischemic damage has occurred subsequent to occlusion. Also seen in this image is the evidence of hemorrhage.

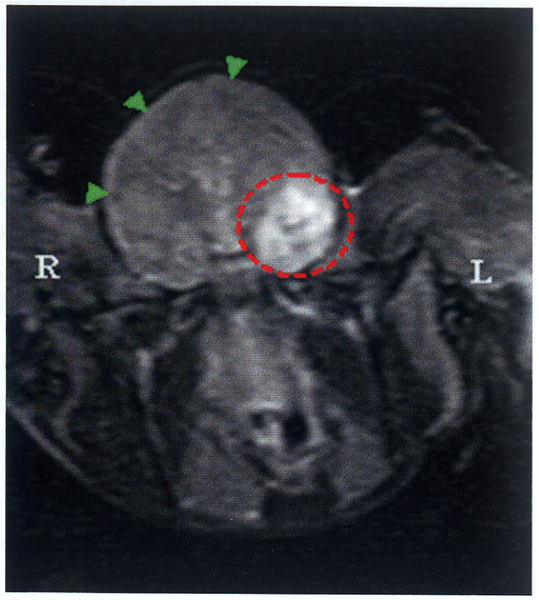

Fig. 9 Postsurgical coronal FLAIR MRI sequences (slice locations: left—L, right—R) confirm onset of ischemia (*dotted circle*) in the left temporal and inferior frontal lobe following the production of a period of left MCA occlusion. Images also confirm the presence of subarachnoid hemorrhage (indicated by *green arrowheads*)

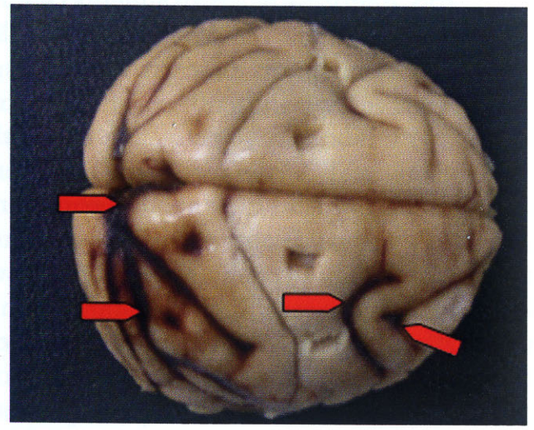

Fig. 10 Gross pathology (indicated by *red arrows*) of the dorsal surface of the brain, illustrating SAH

Figure 10 shows gross examination results confirming that a SAH is present bilaterally in the depths of the sulci over the dorsal aspect of the brain. An ill-defined area of pallor and blurring of the gray–white junction, consistent with edema subsequent to ischemia, were identified in the superior temporal gyrus and posterior hippocampus (results not shown).

4 Conclusions

Disturbances in brain function can have immediate, severe, and lifelong consequences. Therefore, monitoring activity of the brain holds considerable significance in a broad range of clinical fields such as neonatology, psychiatry, gerontology, emergency care, neurology, physical rehabilitation, and surgery. Diffuse optical imaging, deployed to yield topographic or tomographic information, has emerged as a promising, versatile method. We hope, by means of the review of the methodology presented in this chapter, to encourage and spur others to adopt it for different applications. As outlined here, the tomography method can resolve different forms of hemodynamic events having clinical significance, and yields information that is strongly corroborated by standard independent measures.

The distillation of methods for clinical application requires consideration of many factors beyond what is necessary to support investigative studies. World-wide, there are hundreds of laboratories using NIRS tomography and topography systems in support of clinical investigative studies. At present, the method remains experimental. However, the favorable attributes of a compact and versatile technology footprint, and its use of non-damaging energy sources, together with continued development in advanced processing environments [see Notes 4 and 5], strongly favor development of useful clinical applications. It is also recognized that, similar to other neuroimaging methods, it can be desirable to merge technologies in order to extend their overall sensing capabilities. Of special interest is the capacity to merge NIRS studies with EEG. Time-series measures, in general, are rich in information and expected improvements to system design and integration should serve to significantly extend their utility. Direct evidence of this is a recent report that showed improved performance of brain–computer interface applications [46] from concurrent NIRS-EEG measures. Additionally, advances in data analysis [47] and modeling [48] have shown promise for extending the information content accessible from NIRS measures.

To date, most multichannel NIRS topography and tomography studies focus primarily on brain-function applications [49–53]. Many multichannel NIRS topography applications have been developed [54–56], and the method has already been shown to detect brain ischemia and hemorrhage [57–60]. For example, this has been accomplished by using topographic (2D) absorption images in a newborn piglet model (16 sources, 2 detectors) [61]. While NIRS topography clinical applications may have illustrated the capability and importance of detecting such phenomena, the 3D localization of such entities is still lacking. In our study, we have illustrated that the temporal and spatial features seen in the reconstructed 3D image time series faithfully coincide with the observed events.

5 Author's Notes on Optical Imaging: Solutions to Common Problems

In this section we discuss solutions to some of the problems one may encounter when implementing the methodology described in this chapter.

Note 1: *Topography* vs. *Tomography*: This is a frequently considered issue. Favoring the use of the former is a sparser sensing arrangement and consequently the capacity for greater surface coverage. A notable concern for topography studies, however, is the evidence that scalp contributions can significantly bias estimates of true cortical responses, and that in some cases these biases dominate [62]. Having a larger dynamic range, tomography systems allow for a denser sensor arrangement. Shorter distance source–detector arrangements preferentially probe near-surface tissue volumes. The use of this information to account for scalp contributions is directly considered by model-based image reconstruction methods. More simplified empirical strategies (e.g., simple regression) can be employed to remove or account for near-surface tissue information, but because the sensitivity of the measurement to underlying features is strongly nonlinear, such strategies can distort information. As discussed more fully in Notes 4 and 5, implementation of a tomography approach requires access to thoughtfully considered analysis software. At present, these are not commercially available, although university-based freeware resources can be found at www.nitrc.org.

Note 2: *Optode–Tissue Interface*: Note 1 mentions biases originating from vascular responses occurring in the scalp. In the study described in this chapter, this concern was largely avoided because the scalp and underlying muscle tissue was surgically resected. However, two additional considerations remain. First is the need to mechanically stabilize the sensing array. This is important because even small variations in mechanical stability can cause artifacts. Here, stability was achieved by introducing screws to lock down the array. Second, while removal of the overlying tissues significantly improves sensitivity to deeper-lying structures, it affects the boundary conditions that apply to the forward and inverse modeling computations. To overcome this concern, when performing these computations using the developed hybrid atlas, the position of the sensing array was assigned to the surface of the skull rather than to the scalp.

In noninvasive studies (such as those performed on humans), consideration of the optode–tissue interface has added importance when the measurements are performed at sites where hair is present. Darkly pigmented hair, in particular, is a strong optical attenuator and must be displaced to ensure high-quality measures. One solution is to use small-diameter optodes that can fit between the hair follicles. While effective, this raises two other concerns. First, signal levels scale with the sensor aperture. Second, extended contact with small-diameter optodes can become notably uncomfortable

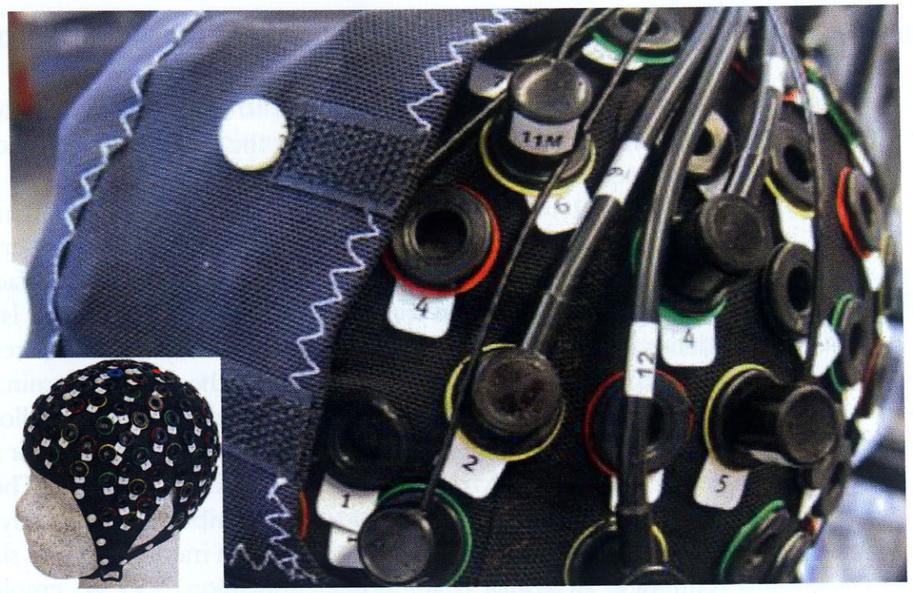

Fig. 11 View of the modified EEG cap showing LED sources and detection fibers, and a portion of the over-cap

due to the induction of scalp ischemia. A simple solution is to use optodes having a larger contact surface area. This can pose added efforts for hair displacement, but we have found the use of hair gel prevents the displaced hair from reverting to its original location. In our experience, optodes having a diameter of 3 mm can be worn for extended periods of time (at least 2 h).

A related issue is the profile of the optodes. Commonly considered is the use of spring-load optode housings. These are effective in stabilizing the sensing array against small-amplitude head movements. Unfortunately, these designs impose a higher profile on the optodes (i.e., they protrude farther from the scalp), rendering the array more susceptible to inertial forces produced by head movements. One solution that we have found effective is to employ a double-layered cap design consisting of an elastomeric under-cap (of the type commonly used in EEG studies) into which optode holders and optodes are introduced. This array is then covered by an over-cap which also has elastomeric properties (see Fig. 11). This approach confers three advantages. First is that it supports the use of low-profile optode designs, thereby reducing susceptibility to inertial forces and helping to ensure constant optode contact with the scalp. Second, the over-cap produces a more uniform distribution of force onto the head, improving subject comfort. Third, for optical measures that are sensitive to ambient light, the use of darkly colored caps serves as an effective light shield.

Note 3: *Illumination-Detection Strategies*: Mainly, the considerations discussed in this note are factors hard-wired into system design and consequently are not easily changed. We include this material because it is our experience that those who are not closely aligned with the biomedical optics community frequently are unsure of the trade-offs inherently associated with the many approaches available to system designers.

1. Optical Detectors: Three widely available sensors for optical measurements are silicon photodiodes, avalanche photodiodes, and photo-multiplier tubes. The second and third have greater sensitivity to low light signals, but add to system cost, complexity, and form-factor size. Silicon photodiodes are inexpensive, small, have a large linear dynamic range, and are increasingly the sensor of choice, especially where the aim is to deploy wearable devices [63].
2. Optical Sources: Measures performed in the NIR region are frequently accomplished using either LEDs (light-emitting diodes) or laser diodes. Laser diodes offer a significantly narrower emission profile (typically 2–3 nm full-width at half-maximum) relative to LEDs, especially at wavelengths >900 nm, but are more sensitive to damage from voltage instabilities and can require active temperature control to achieve acceptable stability. For studies involving measures of the Hb signal (690–850 nm range), the two source types can yield nearly equivalent information. However, in cases where resolution of endogenous chromophores in addition to Hb is desired (e.g., detection of lipid, water signal in the 900–1,000 nm range), the use of laser diodes are preferred owing to the notably narrower emission profile.
3. Combined Illumination-Detection Strategies: There are two principal considerations that frequently arise. One of these concerns the type of information that is being sought. Frequency- and time-domain measures are methods sensitive to the absolute background concentration of Hb and other constituents that absorb radiation at the employed wavelengths, as well as to the scattering properties of tissue [32]. Compared to the more simplified instrumentation employed with continuous wave (CW) methods (the type that is used here), these methods do have the potential to yield additional information beyond that easily obtained with CW methods. Nevertheless, the instrumentation required for such measures is notably more costly than CW, and not easily adapted to wearable systems. Some investigators have asserted that it is possible to obtain "absolute" measures of the Hb signal in tissue, particularly with respect to frequency-domain measures. However, the fact is that the complexity of tissue (e.g., the differing optical properties of each tissue layer) assures that, without considerable additional computational effort, the Hb quantities obtained are not actually absolute, but are convolved in a complex manner whose relationship to the true value is

not easily discerned. Nevertheless, these methods do offer the advantage of providing measurement signals (time-domain: temporal point spread function; frequency-domain: frequency-dependent amplitude and phase [24]), while CW measurements are restricted to the overall light intensity only. The second consideration related to combined source–detector measures is the arrangement of the optode array in relation to the expected location of the target area. A simple approach often used for topographic studies is to arrange the sources and detectors in an alternating pattern, usually separated by ~3 cm. This separation distance allows for at least a portion of the light to interact with cortical structures. Evidence of this interaction is gained from the presence of a cardiac signal in the data. In fact, the latter signal, while ordinarily taken as evidence of light interacting with arterial structures, in the brain is mainly evidence of brain motion due to mechanical forces resulting from ventricular contraction of the heart. In cases where multi-distance measures are desired (particularly for tomography), the decision on how best to arrange the array can depend on other factors, one of which is the influence that other optical sources may have on the detected signal (e.g., optical cross talk; see report by Al abdi et al. [64] for helpful suggestions).

Note 4: *Approaches to Forward Modelling*: The need for forward modelling arises primarily in cases where the aim is to perform tomography. In fields such as EEG, this problem is often dealt with by using analytic or approximate analytic solvers that are computationally efficient. Similar approaches can also be considered for the NIRS problem, but the many tissue layers (e.g., scalp, muscle, bone, meninges, cortex, sub-cortical white matter) of the head and the frequent influence of local events on the detected signal tend to argue for use of more accurate but computationally intensive methods. The approach we and others [65] have adopted for forward modeling is to employ a 3D finite element solver to compute numerical solutions to the diffusion equation. This and the related topic of inverse methods (see Note 5) can be nontrivial to implement. Fortunately, teams, including ourselves, have made efforts to create packaged solutions that are straightforward to use and are readily available (for example, visit www.nitrc.org).

A straightforward simplification is to pre-compute required information for a large number of possible illumination-detection conditions from a head model, thereby establishing a large look-up table. We have implemented this approach for most locations on the adult head (see Sect. 2.5) and for the hybrid atlas used here. Still, we are aware that more flexible solutions are desirable (e.g., efficient evaluation of subject-based DICOM images, precomputed tables for standard atlases, etc.). To this end, the implementation of fast and

efficient computing strategies based on GPU (Graphical Processing Units) processing strategies is becoming increasingly feasible [66].

Note 5: *Limitations of Linear Inverse Solvers Applied to Time-Series Measures.* A standard approach for solving inverse problems is to employ recursive methods that repeatedly update intermediate forward and inverse solutions [67]. While this can lead to accurate findings, it remains thoroughly impractical when applied to a time series, especially if analytic solvers are not employed. Fortunately, at least for situations where the goal is to define relative changes, first-order linear solvers (which are less computationally intensive than recursive methods) provide for accurate recovery of the temporal information and usefully accurate spatial information, even for complex media [68, 69]. This is the approach adopted here, where the qualitative accuracy of the optical inverse-problem results is corroborated by independent validation methods. The computational methods used are very efficient, with inversion of a dataset consisting of several thousand time frames requiring only a few minutes using a I7-processor. Nevertheless, details of these types of solutions are beyond what most would care to consider. This emphasizes the need for a well-constructed and documented advanced computing environment, such as the one that we continue to develop.

Acknowledgements

This research was supported in part by the National Institutes of Health (NIH) under Grants nos. R21NS067278, R42NS050007, and 5R44NS049734; by Defense Advanced Research Projects Agency project N66001-10-C-2008; and by the Empire Clinical Research Investigator Program (ECRIP) of the New York State Department of Health.

References

1. Updated mild traumatic brain injury guideline for adults: a part of CDC's "Heads Up" series. http://www.cdc.gov/concussion/pdf/TBI_Clinicians_Factsheet-a.pdf
2. Saunders D, Jäger HR, Murray AD, Stevens JM (2008) Skull and brain: methods of examination and anatomy. In: Grainger RC, Allison D, Adam, Dixon AK (eds) Diagnostic radiology: a textbook of medical imaging, 5th edn. Churchill Livingstone, New York, Chapter 55
3. Wilkinson ID, Paley MNJ (2008) Magnetic resonance imaging: basic principles. In: Grainger RC, Allison D, Adam A, Dixon AK (eds) Diagnostic radiology: a textbook of medical imaging, 5th edn. Churchill Livingstone, New York, Chapter 5
4. Klunk WE, Engler H et al (2004) Imaging brain amyloid in Alzheimer's disease with Pittsburgh Compound-B. Ann Neurol 55(3): 306–319
5. Stanzione P, Marciani MG, Maschio M, Bassetti MA, Spanedda F, Pierantozzi M, Semprini R, Bernardi G (1996) Quantitative EEG changes in non-demented Parkinson's disease patients before and during L-dopa therapy. Eur J Neurol 3:354–362
6. Castellanos NP, Paúl N, Ordóñez VE, Demuynck O, Bajo R, Campo P, Bilbao A,

Ortiz T, del-Pozo F, Maestú F (2010) Reorganization of functional connectivity as a correlate of cognitive recovery in acquired brain injury. Brain 133:2365–2381

7. Niedermeyer E, da Silva FL (2004) Electroencephalography: basic principles, clinical applications, and related fields. Lippincot Williams & Wilkins, New York. ISBN 0-7817-5126-8
8. Swartz BE (1998) The advantages of digital over analog recording techniques. Electroencephalogr Clin Neurophysiol 106(2):113–117
9. Hansen PC, Kringelbach ML, Salmelin R (eds) (2010) MEG: an introduction to methods. Oxford University Press Inc., New York
10. Lindauer U, Gethmann J, Kühl M, Kohl-Bareis M, Dirnagl U (2003) Neuronal activity-induced changes of local cerebral microvascular blood oxygenation in the rat: effect of systemic hyperoxia or hypoxia. Brain Res 975(1–2): 135–140
11. Bailey DL, Townsend DW, Valk PE, Maisey MN (2005) Positron emission tomography: basic sciences. Springer, Secaucus, NJ. ISBN 1-85233-798-2
12. Buxton RB (2002) Introduction to functional magnetic resonance imaging: principles and techniques. Cambridge University Press, Cambridge. ISBN 0-521-58113-3
13. Cabeza R, Kingstone A (eds) (2006) Handbook of functional neuroimaging of cognition, 2nd edn. MIT Press, Cambridge, MA. ISBN 0-262-03344-5
14. Moonen CTW, Bandettini PA (eds) (2000) Functional MRI. Springer, New York, Chapters 9–11
15. Blas ML, Lobato EB, Martin T (1999) Noninvasive infrared spectroscopy as a monitor of retrograde cerebral perfusion during deep hypothermia. J Cardiothorac Vasc Anesth 13(2):244–245
16. Prabhune A, Sehic A, Spence PA, Church T, Edmonds HL Jr (2002) Cerebral oximetry provides early warning of oxygen delivery failure during cardiopulmonary bypass. J Cardiothorac Vasc Anesth 16(2):204–206
17. Davie SN, Grocott HP (2012) Impact of extracranial contamination on regional cerebral oxygen saturation: a comparison of three cerebral oximetry technologies. Anesthesiology 116(4):834–840
18. Slater JP, Guarino T, Stack J, Vinod K, Bustami RT, Brown JM III, Rodriguez AL, Magovern CJ, Zaubler T, Freundlich K, Parr GV (2009) Cerebral oxygen desaturation predicts cognitive decline and longer hospital stay after cardiac surgery. Ann Thorac Surg 87(1):36–44, discussion 44–5
19. Edmonds HL Jr, Ganzel BL, Austin EH III (2004) Cerebral oximetry for cardiac and vascular surgery. Semin Cardiothorac Vasc Anesth 8(2):147–166
20. Ma H, Zhao M, Schwartz TH (2013) Dynamic neurovascular coupling and uncoupling during ictal onset, propagation, and termination revealed by simultaneous in vivo optical imaging of neural activity and local blood volume. Cereb Cortex 23(4):885–899
21. Jobsis FF (1977) Noninvasive, infrared monitoring of cerebral and myocardial oxygen sufficiency and circulatory parameters. Science 198:1264–1267
22. Barbour RL, Graber HL, Aronson R, Lubowsky J (1990) Model for 3-D optical imaging of tissue. International geoscience and remote sensing symposium (IGARSS), vol 2, pp 1395–1399
23. Barbour RL, Lubowsky J, Graber HL (1988) Use of reflectance spectrophotometry as a possible 3-dimensional spectroscopic imaging technique. FASEB J 2:a1772
24. Graber HL, Chang J, Aronson R, Barbour RL (1993) A perturbation model for imaging in dense scattering media: derivation and evaluation of imaging operators. In: Mueller GJ, Chance B, Alfano RR, Arridge SR, Beuthan J, Gratton E, Kaschke M, Masters BR, Svanberg S, van der Zee P (eds) Medical optical tomography: functional imaging and monitoring, vol IS11. Society of Photo-Optical Instrumentation Engineers, Bellingham, WA, pp 121–143
25. Arridge SR (1999) Optical tomography in medical imaging. Inverse Probl 15(2):R41–R93
26. Colier W, Quaresima V, Barattelli G, Cavallari P, van der Sluijs M, Ferrari M (1997) Detailed evidence of cerebral hemoglobin oxygenation in response to motor cortical activation revealed by a continuous wave spectrometer with 10 Hz temporal resolution. Proc SPIE 2979:390–396
27. Delpy DT, Cope M (1997) Quantification in tissue near-infrared spectroscopy. Philos Trans R Soc Lond B Biol Sci 352:649–659
28. Eda H, Oda I, Ito Y, Wada Y, Oikawa Y, Tsunazawa Y, Takada M, Tsuchiya Y, Yamashita Y, Oda M, Sassaroli A, Yamada Y, Tamura M (1999) Multichannel time-resolved optical tomographic imaging system. Rev Sci Instrum 70:3595–3602
29. Gratton E, Mantulin WW, vandeVen MJ, Fishkin JB, Maris MB, Chance B (1993) A novel approach to laser tomography. Bioimaging 1:40–46
30. Hock C, Villringer K, Müller-Spahn F, Wenzel R, Heekeren H, Schuh-Hofer S, Hofmann M, Minoshima S, Schwaiger M, Dirnagl U, Villringer A (1997) Decrease in parietal cerebral hemoglobin oxygenation during performance of a verbal fluency task in patients with Alzheimer's disease monitored by means of near-infrared spectroscopy (NIRS)-correlation with simultaneous rCBF-PET measurements. Brain Res 755:293–303
31. Villringer A, Chance B (1997) Non-invasive optical spectroscopy and imaging of human brain function. Trends Neurosci 20:435–442
32. Ferrari M, Quaresima V (2012) A brief review on the history of human functional near-infrared spectroscopy (fNIRS) development and fields of application. Neuroimage 63:921–935
33. Koizumi H, Yamamoto T, Maki A, Yamashita Y, Sato H, Kawaguchi H, Ichikawa N (2003) Optical topography: practical problems and new applications. Appl Opt 42:3054–3062
34. Piper SK, Krueger A, Koch SP, Mehnert J, Habermehl C, Steinbrink J, Obrig H, Schmitz CH (2014) A wearable multi-channel fNIRS system for brain imaging in freely moving subjects. Neuroimage 85(pt 1):64–71
35. Fish RE, Brown MJ, Danneman PJ, Karas AZ (2008) Anesthesia and analgesia in laboratory animals. Elsevier Inc., San Diego, CA. ISBN 978-0-12-373898-1
36. Schmitz CH, Löcker M, Lasker JM, Hielscher AH, Barbour RL (2002) Instrumentation for fast functional optical tomography. Rev Sci Instrum 73:429–439
37. Schmitz CH, Graber HL, Pei Y, Farber MB, Stewart M, Levina RD, Levin MB, Xu Y, Barbour RL (2005) Dynamic studies of small animals with a four-color DOT imager. Rev Sci Instrum 76:094302
38. Scholkmann F, Wolf M (2013) General equation for the differential pathlength factor of the frontal human head depending on wavelength and age. J Biomed Opt 18(10):105004
39. Schmitz CH, Klemer DP, Hardin RE, Katz MS, Pei Y, Graber HL, Levin MB, Levina RD, Franco NA, Solomon WB, Barbour RL (2005) Design and implementation of dynamic near-infrared optical tomographic imaging instrumentation for simultaneous dual-breast measurements. Appl Optics 44:2140–2153
40. Xu Y, Ewald A, Graber HL, Nichols JD, Pflieger ME, Ossadtchi A, Schmitz CH, Barbour RL (2012) A computing environment for multimodal integration of EEG and fNIRS. Poster 46 at functional near infrared spectroscopy, London, UK, 26–28 October 2012
41. Graber HL, Xu Y, Pei Y, Barbour RL (2005) Spatial deconvolution technique to improve the accuracy of reconstructed three-dimensional diffuse optical tomographic images. Appl Optics 44:941–953
42. Xu Y, Graber HL, Barbour RL (2007) An image correction algorithm for functional 3D DOT brain imaging. Appl Optics 46:1693–1704
43. Barbour RL, Graber HL, Xu Y, Pei Y, Schmitz CH, Pfeil DS, Tyagi A, Andronica R, Lee DC, Barbour S-LS, Nichols JD, Pflieger ME (2012) A programmable laboratory testbed in support of evaluation of functional brain activation and connectivity. IEEE Trans Neural Syst Rehabil Eng 20:170–183
44. McLaren DG, Kosmatka KJ, Oakes TR, Kroenke CD, Kohama SG, Matochik JA, Ingram DK, Johnson SC (2009) A population-average MRI-based atlas collection of the rhesus macaque. Neuroimage 45:52–59
45. Okamoto M et al (2005) Spatial registration of multichannel multi-subject fNIRS data to MNI space without MRI. NeuroImage 27: 842–851
46. Fazil S, Mehnert J, Steinbrink J, Curio G, Villringer A, Muller KR, Blankertz B (2012) Enhanced performance by a hybrid NIRS-EEG brain computer interface. Neuroimage 59: 519–529
47. Wylie GW, Graber HL, Voelbel GT, Kohl AD, DeLuca J, Pei Y, Xu Y, Barbour RL (2009) Using co-variations in the Hb signal to detect visual activation: a near infrared spectroscopic imaging study. Neuroimage 47:473–481
48. Fantini S et al (2013) Dynamic model for the tissue concentration and oxygen saturation of hemoglobin in relation to blood volume, flow velocity and oxygen consumption: implications for functional neuroimaging and coherent hemodynamic spectroscopy (CHS). Neuroimage S1053–8199(13):00315–00317
49. Chen S et al (2002) Auditory-evoked cerebral oxygenation changes in hypoxic-ischemic encephalopathy of newborn infants monitored by near infrared spectroscopy. Early Hum Dev 67:113–121
50. Okamoto M et al (2006) Prefrontal activity during taste encoding: an fNIRS study. Neuroimage 47(2):220–232
51. Holper L, Muehlemann T, Scholkmann F, Eng K, Kiper D, Wolf M (2010) Testing the potential of a virtual reality neurorehabilitation system during performance of observation, imagery and imitation of motor actions recorded by wireless functional near-infrared spectroscopy (fNIRS). J Neuroeng Rehabil 7:57
52. White BR, Culver JP (2010) Quantitative evaluation of high-density diffuse optical tomography: in vivo resolution and mapping performance. J Biomed Opt 15:026006

53. Habermehl C, Holtze S, Steinbrink J, Koch SP, Obrig H, Mehnert J, Schmitz CH (2012) Somatosensory activation of two fingers can be discriminated with ultrahigh-density diffuse optical tomography. Neuroimage 59: 3201–3211
54. Hyde DC, Boas DA, Blair C, Carey S (2010) Near-infrared spectroscopy shows right parietal specialization for number in pre-verbal infants. Neuroimage 53:647–652
55. Nakahachi T, Ishii R, Iwase M, Canuet L, Takahashi H, Kurimoto R, Ikezawa K, Azechi M, Kajimoto O, Takeda M (2010) Frontal cortex activation associated with speeded processing of visuospatial working memory revealed by multichannel near-infrared spectroscopy during Advanced Trail Making Test performance. Behav Brain Res 215:21–27
56. Kameyama M, Fukuda M, Yamagishi Y, Sato T, Uehara T, Ito M, Suto T, Mikuni M (2006) Frontal lobe function in bipolar disorder: a multichannel near-infrared spectroscopy study. Neuroimage 29:172–184
57. Stankovic MR, Maulik D, Rosenfeld W, Stubblefield PG, Kofinas AD, Gratton E, Franceschini MA, Fantini S, Hueber DM (2000) Role of frequency domain optical spectroscopy in the detection of neonatal brain hemorrhage—a newborn piglet study. J Matern Fetal Med 9(2):142–149
58. Leistner S et al (2011) Non-invasive simultaneous recording of neuronal and vascular signals in subacute ischemic stroke. Biomed Tech (Berl) 56:85–90
59. Zweifel C et al (2010) Continuous assessment of cerebral autoregulation with near-infrared spectroscopy in adults after subarachnoid hemorrhage. Stroke 41:1963–1968
60. Salonia R, Bell MJ, Kochanek PM, Berger RP (2012) Cerebral hemorrhage / ischemia in DOT the utility of near infrared spectroscopy in detecting intracranial hemorrhage in children. J Neurotrauma 29(6):1047–1053
61. Stankovic MR, Maulik D, Rosenfeld W, Stubblefield PG, Kofinas AD, Drexler S, Nair R, Franceschini MA, Hueber D, Gratton E, Fantini S (1999) Real-time optical imaging of experimental brain ischemia and hemorrhage in neonatal piglets. J Perinat Med 27: 279–286
62. Takahashi T, Takikawa Y, Kawagoe R, Shibuya S, Iwano T, Kitazawa S (2011) Influence of skin blood flow on near-infrared spectroscopy signals measured on the forehead during a verbal fluency task. Neuroimage 57: 991–1002
63. Strangman G, Boas DA, Sutton JP (2002) Non-invasive neuroimaging using near-infrared light. Biol Psychiatry 52:679–693
64. Al abdi R, Graber HL, Xu Y, Barbour RL (2011) Optomechanical imaging system for breast cancer detection. J Opt Soc Am A Opt Image Sci Vis 28:2473–2493
65. Kak AC, Slaney M (1999) Principle of computerized tomographic imaging, classics in applied mathematics. SIAM, Philadelphia, PA
66. Fang Q, Boas DA (2009) Monte Carlo simulation of photon migration in 3D turbid media accelerated by graphics processing units. Opt Express 17(22):20178–20190
67. Dehghani H, Eames ME, Yalavarthy PK, Davis SC, Srinivasan S, Carpenter DM, Pogue BW, Paulsen KD (2008) Near infrared optical tomography using NIRSFAST: algorithm for numerical model and image reconstruction. Comm Numer Meth Eng 25:711–732
68. Pei Y, Graber HL, Barbour RL (2001) Influence of systematic errors in reference states on image quality and on stability of derived information for DC optical imaging. Appl Optics 40:5755–5769
69. Graber HL, Pei Y, Barbour RL (2002) Imaging of spatiotemporal coincident states by DC optical tomography. IEEE Trans Med Imaging 21:852–866

INDEX

Mingrui Zhao et al. (eds.), *Neurovascular Coupling Methods*, Neuromethods, vol. 88,
DOI 10.1007/978-1-4939-0724-3, © Springer Science+Business Media New York 2014